Climatology of Melting Layer Heights Estimated from Cloud Radar Observations at Various Locations

Jae In Song[1, 2], Seong Soo Yum[1], Sung-Hwa Park[3], Ki-Hoon Kim[3], Ki-Jun Park[3], Sang-Won Joo[3]

Affiliations:

[1]. Department of Atmospheric Sciences, Yonsei University, Seoul 03722, Korea

[2]. Department of Future & Smart Construction Research, Korea Institute of Civil Engineering and Building Technology (KICT), Gyeonggi-do 10223, Korea

[3]. National Institute of Meteorological Sciences, Korea Meteorological Administration, Jeju-do 63566, Korea

Revised for publication in Journal of Geophysical Research-Atmospheres

May 2021

Corresponding author: Dr. Seong Soo Yum (ssyum@yonsei.ac.kr)

Key Points:

- A melting layer detection algorithm for Ka-band cloud radar is developed and shows good agreement with the reanalysis data.
- The occurrence frequency and the height of the melting layer at five different sites exhibit different environmental characteristics.
- Two newly introduced indices well represent the thermodynamic characteristics of clouds that have a melting layer.

Abstract

A melting layer (ML) detection algorithm for cloud radar with polarimetric capability was developed and applied to the cloud radar data collected from five different sites around the world for several years. The retrieved melting layer top height (MLH) showed a very good correspondence with the ECMWF Reanalysis 5 (ERA5) zero degree level data for all five sites. Th e ML characteristics were distinctively different for different sites, revealing climatological characteristics of ML forming clouds in different regions. Generally, ML tended to occur more frequently in summer than in winter except for a maritime site, where low stratiform clouds formed frequently in summer, the top of which might be lower than the freezing level. In contrast, at two arctic sites, ML occurred almost exclusively in summer because it was too cold to have an ML in the other seasons. The MLH also varied significantly from site to site but generally higher during warmer seasons. Based on MLH, two new indices, bulk temperature lapse rate (BLR) and relative depth of liquid cloud below MLH (RD) were developed, which were useful to explain the environmental characteristics of the five sites. BLR generally increased with the surface temperature at all sites except at the marine site that showed an opposite trend, where a unique synoptic pattern in winter generated high BLR in this cold season. These findings confirm that studies on thermodynamic structures using cloud radars can be broadened, taking advantage of BLR and RD information, as these indices can represent environmental thermodynamic characteristics of the clouds that have ML.

1. Introduction

Melting layer (ML) is the layer where ice particles turn into raindrops, located nearby 0 □ isotherm level. The depth of ML varies only a few hundred meters while its top height may vary several kilometers (Shin et al. 2000; Matrosov 2008). The ML depth is determined by the presence of unrimed or rimed ice particles and their vertical velocities, precipitation intensity, cloud microphysics, and environmental conditions (Fabry and Zawadzki, 1995; Wolfensberger et al., 2016; Carlin and Ryzhkov, 2019). In contrast, ML top height (MLH) is determined by surface temperature, RH of the air and environmental lapse rate of the atmosphere (Heymsfield et al., 2021). So, MLH varies with latitude and thermodynamic conditions and may differ by the location. Therefore, thermodynamic conditions below ML of stratiform clouds can be revealed by investigating MLH at various sites.

One of the most important features of ML is that it can be easily detected by radar observations because radar reflectivity is enhanced at ML for most radars except for W-band radars (Kollias and Albrecht, 2005). In addition to the enhancement of reflectivity, high differential reflectivity (Z_{DR}) and low copolar correlation coefficient (ρ_{HV}) appear at ML. Using these scattering characteristics, ML detection methods for weather radars (S, C, or X-band radars) have been developed and studied by several researchers (Fabry and Zwadzki, 1995; Hogan and O'Connor 2004; Ikeda et al., 2005; Giangrande et al., 2008; Boodoo et al., 2010; Matrosov et al. 2017). Meanwhile, ML detection methods for spaceborne radars also have been developed for Tropical Rainfall Measurement Mission (TRMM), CloudSat, and Global Precipitation Measurement (GPM) satellites (Shin et al., 2000; Sassen et al., 2007; Le and Chandrasekar, 2012). Yet, the ML detection method for ground-based cloud radar has been infrequently investigated.

Cloud radars utilizing shorter wavelengths (i.e., Ka or W-band) than conventional weather radars are sensitive enough to detect relatively small cloud hydrometeors with high spatiotemporal

resolution. Usually, the spatial resolution of cloud radar is between 5 and 100 m, and temporal resolution can be a few seconds to several minutes depending on the operation strategy. These strengths facilitated various studies that required detailed cloud data, which were impossible for conventional weather radars. First, detailed cloud structure can be revealed by radar reflectivity from hydrometeor particles including cloud droplets (Frisch et al., 1995; Liu et al., 2008). Second, the movement of hydrometeor particles including cloud droplets can be observed and analyzed by using Doppler technique, which is capable of detecting radial movement (Kollias and Albrecht, 2000; Kollias et al., 2001; Kollias et al, 2002; Luke and Kollias, 2013). Third, the phase of cloud particles can also be investigated, albeit limitedly, in association with the bright band that forms due to different scattering characteristics of ice and liquid hydrometeors (Fabry and Zawadzki, 1995; Matrosov, 2005; Matrosov, 2008; Shupe, 2007).

Several institutions have operated cloud radars for decades to take advantage of these merits. The Atmospheric Radiation Measurement (ARM) program run by the United States Department of Energy (DOE) is one of the largest observation programs, operating multiple measurement sites (Mather and Voyles, 2013). The High Definition Clouds and Precipitation for Advancing Climate Prediction [HD(CP)2] program also operates several observatories that are equipped with cloud radars, such as, Jülich Observatory for Cloud Evolution (JOYCE) and Leipzig Aerosol and Cloud Remote Observations System (LACROS) in Germany (Bühl et al., 2013; Löhnert et al., 2015). In addition to such programs, cloud radars have also been operating at Chilbolton (United Kingdom; Wood et al., 2009), Boseong (South Korea; Oh et al., 2016), and Milešovka Mountain (Czech Republic; Sokol et al., 2018), and at some other places.

In this study, we investigated the characteristics of the ML that were observed by cloud radars in various environments for a long period (about 30 years in total data, observation period of each site is presented in Section 2). The data used in this study were obtained from several ARM sites and Boseong Standard Weather Observatory (BSWO). Since different environments generate different

cloud and precipitation characteristics (Khain et al., 2005), the variety of observational sites may represent the climatology of the ML in various environments. To investigate the ML in various environments, we first established a new quality control (QC) method for BSWO data to make them as reliable as the ARM data, the QC method of which was established in several previous studies (Clothiaux et al., 1999; Kollias et al., 2007). Moreover, we developed a melting layer detection algorithm. Both the QC method and the ML detection algorithm are designed for application to any polarimetric cloud radar. Then the retrieved ML height data were analyzed for each observation site. Descriptions of the data and methods employed in this study are introduced in Section 2, followed by the results and discussions in Sections 3 and 4, and the conclusions of this study are in Section 5.

2. Data and Method

The ARM program has been operating cloud radars and other observation instruments in various locations: the Southern Great Plains (SGP) site in Oklahoma was established in 1993 and several other sites were subsequently followed. Benefitting from various instruments that were installed along with cloud radar at the ARM sites, clouds can be thoroughly investigated with a holistic approach. Two types of cloud radars have been operating since 1996: millimeter wave cloud radar (MMCR; Kollias et al., 2007) and Ka-band ARM zenith pointing cloud radar (KAZR; Widener et al., 2012). KAZR, a more recent type of cloud radar, is a polarimetric radar, but, MMCR, the older cloud radar, is not. To utilize polarimetric radar capability, only the KAZR data are investigated in this study (Fig. 1).

In addition to the ARM sites, we also analyzed the cloud radar data obtained from the BSWO for a greater variety of data sources. Established in 2014, the BSWO has been operational by the National Institute of Meteorological Sciences (NIMS) of the Korea Meteorological Administration (KMA). The BSWO are comparable to those from the ARM sites since various instruments are

installed at the BSWO, including a Ka-band scanning cloud radar. The site is in the coastal area of South Korea (Fig. 1), which is under the influence of the East Asian Summer Monsoon during the summertime (EASM; Lau et al., 1987; Wang and Lin 2002). Thus, including the data from BSWO expands the climatological variety of this study. Furthermore, previous studies revealed that convective precipitation around the site is fundamentally different from the convective precipitation that occurs at the SGP site, despite the similar latitudinal locations (Sohn et al., 2013; Song and Sohn 2015).

2.1 ARM data

In the ARM program, an observation strategy has been developed to maximize the efficiency of the cloud radar observation since the first deployment of MMCR. As the technical configurations of the cloud radars have been upgraded, the operation strategy and QC methods have been improved accordingly (Clothiaux et al., 1999; Kollias et al., 2007). Furthermore, the ARM program provides Value Added Products (VAPs), which are comprised of a merged data product of the observations of multiple instruments. Active Remote Sensing of CLouds (ARSCL; Clothiaux et al., 2001; Jensen, 2012) and ARM Best Estimation (ARMBE; Chen and Xie, 1994) are commonly used cloud radar VAPs because they are considered to be more reliable than the cloud radar data alone. Because of their reliability, KAZR ARMBE data were used in this study for the maximal period of their availability.

The ARM program is operational at multiple sites in various environments. First, the SGP site (established in 1993) represents a mid-latitude continental environment. Second, the Eastern North Atlantic (ENA) site (established in 2013) located on the Graciosa Island in the middle of the Atlantic Ocean, has been operational for the purpose of obtaining meteorological observation of the mid-latitude marine environment. ARM program also monitors polar and tropical environments. North Slope of Alaska (NSA) and the Oliktok point (OLI; temporary mobile facility) sites are established to monitor Arctic climatology in 1997 and 2015, respectively. The Tropical Western Pacific (TWP) site

has been operational since 1996 to monitor tropical atmosphere such as El Niño Southern Oscillation (ENSO). However, the data from TWP are excluded in this study due to the absence of polarimetric cloud radar data. Some details of ARM observational sites are explained by Miller et al. (2016).

We investigated only the data from 4 ARM sites (SGP, ENA, NSA, and OLI) where linear depolarization ratio (LDR) data are available. Except for NSA and OLI, which are expected to show a similar environment due to their proximity, all sites represent distinctively different cloud and precipitation environments. The data from SGP obtained from January 2011 to April 2019 are representative of the data from the continental environment. The data from ENA obtained from July 2015 to April 2019 are representative of the data from the mid-latitude maritime environment. The data from NSA and OLI are gathered from November 2011 to April 2019 and from July 2015 to April 2019, respectively, and they both are representative of the arctic region. Due to the locational proximity of NSA and OLI, their similarity in cloud statistics is expected.

2.2 BSWO data and Quality Control

In contrast to the ARM sites, the BSWO site represents the climatology of a different region. BSWO is in the southern coastal area of the Korean Peninsula, located in the eastern edge of the Eurasian continent under the influence of dominant westerly winds. As a result, the cloud and precipitation system that develops over the BSWO differs from those over marine or continental environments. Precipitation over this region has two distinguishing features. The first is excessive precipitation during the summertime; more than 50% of the yearly precipitation usually comes between June and September (Shin and Lee 2005; Kim and Lee, 2006) driven by the EASM (Wang and Lin 2002; Yihui and Chan, 2005). Another feature is that convective cloud and precipitation systems usually have a lower cloud top height than those that occur over the continental environment, such as the SGP site (Sohn et al., 2013; Song and Sohn 2015). Therefore, the use of BSWO data can expand

the scope of investigation with additional environmental variety of mid-latitude convective systems. The data obtained from October 2014 to November 2017 at the BSWO are analyzed in this study, following detailed specifications and operation schedules introduced by Oh et al. (2018).

Due to the absence of a reliable QC method, such as ARMBE, a new QC method is designed for BSWO cloud radar. An example of a time series of original radar moment data and their contoured frequency by altitude diagram (CFAD) are shown in Fig. 2, where band-shaped horizontal noises and clutters near the ground are indicated by the two red boxes. Oh et al. (2018) and Oh et al. (2019) have attempted to develop a QC method to render observation data reliable. However, the product of their QC method was not very satisfactory. A considerable proportion of the radar echoes from the hydrometeor particles below the altitude of 5 km were often misclassified radar noise and eliminated from the final product. Figure 3 shows the CFAD of the cloud radar data after applying their QC method: the depicted frequency at the CFADs is not continuous, which suggests an error in their QC method.

Radar reflectivity (Z), vertical velocity (V), and linear depolarization ratio (LDR) of radar echo from hydrometeor particles are normally within certain ranges, unlike clutter and/or noise. Thus, we established criteria for distinguishing hydrometeor particles into five types, as indicated in Table 1, based on the previous studies (Gunn and Kinzer, 1949; Sauvageot and Omar, 1987; Frisch et al., 1995; Mace and Sassen, 2000; Baedi et al., 2002; Sato and Okamoto, 2006; Liu et al., 2008). The five types are liquid cloud, ice cloud, low cloud, light precipitation, and heavy precipitation. Among those criteria, thresholds for liquid and ice clouds are applied to t123he echoes above 3 km to effectively classify low level clouds (i.e. boundary layer cluods), and others are applied to the echoes below 3 km. In detail, we designed the upper and lower thresholds for Z, V, and LDR for the five types and tuned them empirically. If any of the five criteria is satisfied (i.e., Z, V, and LDR values are between the upper and lower thresholds listed in Table 1), the echo is determined as valid (echo from hydrometeor particles). Otherwise, the echo is determined as noise/clutter, and then, noise and clutter echoes are removed from

the dataset; thus, only the echoes that are assumed to originate from hydrometeors remain. Note that, the effect of attenuation by raindrops is not considered in our QC method due to the absence of other radar product and raindrop size distribution information. Detailed computer codes of this QC method and their descriptions are available online (github.com/Jaein-Song/cloud_parallel). The time series of Z and the CFAD of QCed data are shown in Fig. 4. We feel that the new QC method is more reliable than the previous method in three aspects: 1. removal of band-shaped noise, 2. removal of low-level clutter, and 3. continuous profile in the upper level (~5 km).

2.3 Melting layer (ML) detection algorithm

Previously developed ML detection methods were mostly designed for conventional weather radars with RHI and/or PPI scans (Giangrande et al. 2008; Cha et al., 2009; Boodoo et al., 2010) and for satellite observations (Shin et al., 2000; Sassen et al., 2007; Le and Chandrasekar, 2012). ML detection methods for the zenith pointing cloud radars have been presented in several studies (Hogan and O'Connor, 2004; Neto et al., 2019; Li and Moisseev, 2020). Yet, they did not present the method and the accuracy of it explicitly, and the methods were only applicable for each radar model they used. Therefore, we suggest a new ML detection method that can be universally applicable for all zenith pointing single polarized cloud radar and the analysis on accuracy of the method.

Even though basic physical principles of the ML detection are identical regardless of radar types, the method has to be modified for cloud radar because of different measurement characteristics between cloud radars and conventional weather radars. First, cloud radar is much more sensitive than conventional weather radars, and thus, signals are attenuated more severely by precipitation particles than those from conventional weather radar. Next, the cloud radars utilized in this study are operated with zenith pointing measurement, not RHI or PPI scans. While previously developed ML detection methods are unavailable to the cloud radar due to the different scanning strategy, vertical scanning has

its own advantage, that is, vertical velocity of particles, a crucial variable for particle identification, is observable, rather than radial velocity. Therefore, it is more challenging to design ML detection method for this type of cloud radar data in three aspects: distinguishing ML not only from rain echoes but also from cloud echoes, detecting ML from weaker signals, and dealing with zenith pointing measurement data.

The ML detection algorithm used in this study utilizes Z, V, LDR, and their vertical gradients. The algorithm starts only if the minimum reflectivity of the profile is greater than -10 dBZ, and then determines multiple ML top height (MLH) candidate based on the height where local maxima of Z and LDR correspond closely enough at the first attempt. Note that, the melting layer without local maximum of reflectivity due to attenuation and non-Rayleigh scattering is undetectable with this method. Then, the top and bottom heights of ML are estimated by the algorithm using the vertical gradient of the V. The algorithm is repeated six times from the start to the end of the radar observation, reducing the threshold and narrowing the search range with repetition based on the median MLH of 20 min interval. Last, the algorithm chooses an ML with the maximum LDR value among the ML candidates. These unique characteristics of the algorithm make it robust and universally applicable. Details of the ML detection algorithm are introduced in the supplemental information with the thresholds for Z, V, LDR and their gradients, with the flowchart that explains the algorithm in detail. The MATLAB code for the algorithm is available online (github.com/jaein-song/ARM_ML).

The ML detection algorithm introduced in this study is designed to be robust and universally applicable with low threshold values and iterative approach. Since cloud radars detect not only precipitation but also clouds, developing the ML detection algorithm for cloud radars is more challenging than that for conventional weather radars: Due to the sensitivity of cloud radars and the nature of their transmitting wavelengths, cloud radars can detect a substantially greater amount of hydrometeor particles and are influenced by the Mie scattering effect. Due to these features of cloud radars, the characteristic physical signatures of ML may not be distinguishable as clearly as those that

appear in conventional weather radar observations. Therefore, we intentionally designed the ML detection algorithm to be very sensitive by setting low thresholds and doing the iterations to detect the ML as sensitively as possible with reliable accuracy. Because our ML detection algorithm does the iteration with low thresholds, the algorithm is applicable to all LDR observable zenith pointing cloud radars.

3. Results

Figure 5a shows the cloud radar observation that detected the ML at the NSA site on September 12, 2013. The white and grey dots indicate the top and the bottom of the ML, respectively. These dots match with the top and bottom of the bright band, where the reflectivity is higher than that from neighboring echoes. Detection failure (not being detected despite the seeming appearance of ML in the Z profile) does not occur in this figure. Inaccurate detection or misestimation of the MLH does not occur as well. The detected ML tops and bottoms are continuous and are not discrete. Figure 5a demonstrates that the proposed algorithm detects and locates the ML successfully.

Figures 5b and 5c illustrate the advantage and disadvantage of ML detection using a Ka-band cloud radar, compared to that using an X-band radar. Only the echoes with reflectivity higher than -10 dBZ in Fig. 5a are presented in Fig. 5b to simulate X-band radar. Note that, the actual observation of precipitation using X-band radar may differ from the simulated results due to the difference in scattering characteristics of each wavelength and sensitivity of the radar. Compared to Fig. 5a, most of the cloud echoes are eliminated in Fig 5b and the number of detected ML is reduced by 8 % in Fig. 5b compared to that in Fig 5a. However, ML detection by Ka-band cloud radar is hampered during the heavy precipitation. Figure 5c displays the cloud radar observation at BSWO on July 17, 2017. Between 1000 UTC and 1200 UTC when rain is heavy with rain rate of 20 mm h^{-1}, radar signal is severely attenuated by precipitation and therefore radar pulse could not reach to the ML level. Because

of that, ML could not be observed by the cloud radar, which would have been observed by a weather radar (i.e., S, C, X band radar). In a nutshell, detectability of ML is higher with cloud radar than with weather radar, but such capability of cloud radar is severely limited during heavy precipitation.

To validate the accuracy of the algorithm, the hourly averaged ML detection results are compared with ECMWF Reanalysis 5 (ERA5) single layer data with a 0.25°×0.25° grid scale. The amount of total data in hours and the ML detected time in hours are presented in Table 2. Since ML indicates the layer where water freezes and melts, it can be validated with the temperature variables of ERA5 data. The zero degree level (ZDL) is a variable that represents the altitude where the temperature is 0 □. At the ML top, where the melting begins, the temperature is nearly 0 □ and the temperature below the ML top is usually higher than 0 □. Therefore, the retrieved ML top height may coincide with the ZDL of ERA5 data. The comparison between them is shown in Fig. 6. Most data exist close to one to one line with very high coefficient of determination (R^2), small negative bias and root mean square error (RMSE), regardless of the site. When RH is lower than 100 %, ice particles would sublimate rather than melt if the ice bulb temperature is lower than 0 □ (Heymsfield et al., 2021). Thus, the level of ice bulb temperature being 0 □, which would be identical to ML top, can be lower than ZDL, and this may explain the small negative bias of the estimated ML top height. Another thing to note is that RMSEs might be overestimated compared to the actual accuracy of the algorithm due to the errors of the ZDL data.

Figure 7 presents seasonal and diurnal variations of cloud occurrence frequencies at all sites. Cloud occurrence was counted when radar echo existed at more than ten pixels in a radar reflectivity profile regardless of the height. Then, cloud occurrence frequency (%) was calculated by dividing the number of cloud occurrences by the total number of observations. Seasonal variations of cloud occurrence frequencies are distinctively different at all sites except that they are similar at NSA and OLI. Diurnal variations, however, are relatively small at all sites. In detail, at SGP clouds occur most in spring and least in the afternoon in summer. In contrast, summer is the time for the most cloud

occurrence at BSWO due to the effect of EASM (Wang and Lin, 2002). At ENA, clouds occur generally much more frequently than at SGP and BSWO owing to the high occurrence of thick and high clouds in winter and marine boundary layer clouds in summer (Dong et al. 2014, Wood et al. 2015). NSA and OLI show the highest cloud occurrence among all sites due to dominantly frequent high RH and low pressure systems (Shupe et al. 2011).

Similarly, ML occurrence frequencies (%) at all sites are calculated as the ratio of the number of ML occurrence to the number of observations that detected clouds (Fig. 8). Note that the numbers are counted only if ML were observed longer than 10 minutes. ML occurrence is relatively high at nighttime in late summer and fall at the SGP site. ML occurrence is the most frequent at BSWO among all sites, scattered throughout the seasons but the highest in the afternoon in August. ML occurrence is the rarest at the ENA site (see the different color scale for ENA in Fig. 8) and almost none in the summertime, due to high occurrence of low stratiform clouds in this marine environment (Wood et al., 2015). Meanwhile, ML occurs only during the summertime at NSA and OLI because it is too cold to have an ML in all other seasons (i.e., subzero temperatures at the surface). The similar seasonal trend of the two sites is considered to be due to the spatial proximity of the two sites.

Figure 9 shows monthly and hourly averaged MLH at all sites. The figure illustrates the general trend of MLH being higher in summer than in other seasons as temperature rises. The maximum height of MLH was the highest at BSWO and the lowest at NSA and OLI. Such differences imply different thermodynamic characteristics at different sites. As expected in Fig. 8, the MLH during the summer cannot be determined reliably at the ENA site because ML occurrence itself is very low during this season. With no ML occurrence in cold seasons (Oct-Apr) at NSA and OLI, MLH data are absent in these seasons.

To investigate the ML characteristics, we examined a new indicator, which is referred to as the bulk temperature lapse rate (BLR):

$$BLR = \frac{T_{SFC}}{MLH} \ , \tag{1}$$

where T_{SFC} is the surface temperature (in Celsius). Assuming that MLH is the height where the temperature becomes zero, BLR can be considered as the temperature lapse rate for the layer from the surface to MLH (equivalently to the height of the freezing level). Although BLR can be estimated only for the cloudy environments that contain ML, it can represent the characteristics of the thermodynamic structure of clouds and precipitation systems for such environments (Kodama et al., 2009). If it is assumed that the clouds that contain ML developed purely adiabatically over a horizontally homogeneous surface, BLR is expected to be larger than the moist adiabatic lapse rate (~ 5 □ km^{-1}) but smaller than the dry adiabatic lapse rate (10 □ km^{-1}). The specific value of BLR may also depend on where the cloud base height (equivalently the lifting condensation level, LCL) is, which, in turn, would be dependent on relative humidity (RH) of the air. However, we find that BLR has a minimal correlation with the RH of the surface air (not shown). Figure 10 shows that BLR is the highest at ENA, and moreover, a significant portion of BLR (60 % in total) was lower than 5 □ km^{-1}, especially at high latitude sites, NSA and OLI. Since BLR cannot be lower than 5 □ km^{-1} during adiabatic ascent of air parcel, this finding suggests that BLR does not simply depend on RH of the surface air and that some diabatic processes, such as surface inversion layer, temperature advection and/or vertical heat transport, are involved. Yet, the influences of diabatic processes are not investigated in this study.

Figure 11 displays BLR as a function of T_{SFC} (2 □ bins). Each color represents a different site, and the bars and circles indicate the interquartile range (IQR) and the median, respectively, for each T_{SFC} bin. The dashed lines in Fig. 11 are the regression lines for the median BLR value for the five sites; the slopes, intercepts, and R^2, residual standard error (RSE) of each line are shown in Table 3. Figure 11 and Table 3 manifest three notable features. First, BLR increases linearly with T_{SFC} at all but the ENA site. The increasing tendencies would be expected, because generally the surface is heated/cooled faster than the atmosphere, and therefore at higher surface temperature, it is more likely to have a higher BLR. The opposing trend of the ENA site seems to be related to the unique

environment of the eastern north Atlantic region: in the winter season, the upper atmosphere is cooled much more than the lower atmosphere because cold Icelandic low cools the high altitude while the Azores high preserves relatively warm air temperature at low altitudes (Wood et al. 2015), inducing higher BLR in the winter season (i.e., low T_{SFC}) than in the other seasons. Second, the relationship between BLR and T_{SFC} at the NSA and OLI sites are almost identical. The similarity of the relationships between the two sites is again due to their environmental similarity because of the proximity of the two sites. Third, SGP and BSWO show a noticeable difference in the relationship between BLR and T_{SFC}, which might imply their different thermodynamic characteristics of cloud and precipitation systems despite their similar latitudinal locations.

For further investigation of BLR, we compared BLR to the relative depth (RD) of liquid cloud below ML:

$$RD = 1 - \frac{LCL}{MLH} \ . \tag{2}$$

Assuming that LCL is equivalent to the cloud base altitude, RD represents the relative portion of the liquid cloud layer in the layer between the surface and MLH, and the layer between MLH and LCL would indicate liquid water regime. RD would be closer to 1 when LCL is lower due to higher humidity. LCL can be calculated simply by the following equation:

$$LCL \ \ (km) = 0.125 \cdot \left(T_{SFC} - T_{D,SFC}\right), \tag{3}$$

where $T_{D,SFC}$ is the dew point temperature at the surface (Romps, 2017). Combining Eq. (1) and Eq. (2), RD can be expressed as a function of BLR and $T_{D,SFC}$:

$$RD = 1 - 0.125 \cdot BLR + 0.125 \cdot \frac{T_{D,SFC}}{MLH} \ . \tag{4}$$

With reconfiguration, BLR can also be expressed in the following way:

$$BLR = 8\left(\frac{T_{SFC}}{T_{SFC} - T_{D,SFC}}\right)(1 - RD). \tag{5}$$

So T_{SFC}-$T_{D,SFC}$ is found to be a critical factor that determines BLR. If T_{SFC}-$T_{D,SFC}$ is small, BLR would be large but a small T_{SFC}-$T_{D,SFC}$ (i.e., high RH at the surface) implies that the surface is close to saturation and therefore LCL would be low and RD would be close to 1, which would then reduce BLR. That is, BLR is not simply determined by the RH at the surface, which may be the reason why BLR has a minimal correlation with the RH of the surface air as mentioned above. Regardless of the moisture condition, however, BLR would be larger when T_{SFC} is higher as illustrated in Fig. 11.

Figure 12 confirms that RD increases as the RH at the surface increases. However, RD shows mixed responses to T_{SFC} variation as shown in Fig. 13: at some sites, RD tends to increase with T_{SFC} but at some other sites RD tends to decrease slightly. Figure 14 displays BLR as a function of RD (averages for bin width 0.2). The slope, intercept and R^2, RSE of the linear regressions in Fig. 11, 12, 13, and 14 are shown in Table 3. It is clear in Fig. 14 that BLR reduces as RD increases as expected. Moreover, as RD becomes close to 1, BLR approaches the moist adiabatic lapse rate at all but the NSA and OLI sites. This is also expected because "RD ~ 1" means that almost the entire layer between the surface and MLH is in cloud and therefore the temperature lapse rate in this layer should be basically moist adiabatic. The low BLR at NSA and OLI for RD being close to 1 seems to be due to the generally low T_{SFC} and the frequent presence of inversion layer near the surface at these two sites.

A close examination of BLR and the relevant parameters at SGP and BSWO reveals some interesting aspects of the thermodynamic characteristics of the two sites. BLR at SGP is significantly higher than that at BSWO when T_{SFC} is relatively high (> 24 □) (Fig. 11). Expectedly from Eq. (5), RD at SGP is smaller than that at BSWO when T_{SFC} is high (> 24 □) (Fig. 13). Meanwhile, it is found that the average value of CAPE at SGP (716 J kg^{-1}) was higher than that at BSWO (500 J kg^{-1}) when T_{SFC} was higher than 24 □. In fact, this may be expected since CAPE would be larger for the atmosphere with a higher temperature lapse rate, and the higher BLR at SGP would certainly be indicative of a higher temperature lapse rate at SGP than at BSWO at the time of high T_{SFC} (> 24 □). Since higher CAPE implies more vigorous convection, clouds and precipitation at SGP would have

been more vigorous than those at BSWO when T_{SFC} was high (> 24 □). T_{SFC} being higher than 24 □ would indicate summertime condition. So in summary, the atmosphere is relatively drier and clouds are formed higher (smaller RD) but they are convectively stronger (larger CAPE) at SGP than at BSWO, where the atmosphere is more humid and cloud base is lower (larger RD) but convection is less vigorous (smaller CAPE) during the summer season when BSWO is under the influence of EASM. This coincides with the findings of the previous studies that compared thermodynamic characteristics of clouds and precipitation in these two regions (Sohn et al., 2013, Song and Sohn, 2015; Song et al., 2017).

4. Discussion

The notable technical achievements of this study are the development of the cloud radar QC method and ML detection algorithm. The merit of our QC method and ML detection algorithm is that they can be ubiquitously applied to any LDR measurable cloud radar. As shown in Fig. 6, the accuracy of ML detection algorithm seems robust regardless of the sites. However, the accuracy of the algorithm became significantly degraded when LDR was not available (not shown). Thus, this algorithm cannot be applied to the data that did not have LDR information, such as the data measured by MMCR. However, we expect that the applicability of this algorithm will increase as polarimetric cloud radars become more common.

The estimated MLH shows good agreement with the ERA5 reanalysis data and with the results from previous studies that analyzed satellite data. The TRMM satellite, which is equipped with Ku-band precipitation radar, and the GPM mission satellite equipped with Dual-Frequency (Ku and Ka band) Precipitation Radar (DPR), can provide spatial ML distribution data. For example, Shin et al. (2000) presented the seasonal and spatial distribution of MLH in the tropical region (-30 °S – 30 °N) using the TRMM measurement data, and the results were validated with GPM data (Gao et al., 2017).

These previous studies suggest that MLHs tend to be higher in summer, which is in agreement with the findings of this study. However, the MLHs that can be estimated from satellite data are limited in latitudinal range (lower latitudes) and temporally discontinuous. In that regard, ML estimation from cloud radars can be more advantageous.

At the ENA site, ML rarely occurs in the summertime, compared to the other seasons (Fig. 8c). Because ML is usually accompanied by convective clouds, such low ML occurrence implies low occurrence of convective clouds during this season. This situation is unique only to the ENA site since all other sites show higher ML occurrence frequency in the summer season. Considering the fact that all other sites are located in a continental region, this result might reveal the effect of maritime cloud climatology. Characteristics of clouds and precipitation systems at the ENA site were investigated by Giangrande et al. (2019), who classified the cloud types into "Low" or "Deep" clouds, based on the cloud radar echo top height with a threshold of 4 km. They showed that in the JJA period, shallow clouds with a low cloud top were frequently observed but convective precipitation was infrequent that might accompany ML, which is generally consistent with the low ML occurrence frequency in the summertime shown in Fig. 8c.

The differences between the clouds and precipitation at BSWO and at SGP not only are consistent with the previous studies that suggested the "warm-type precipitation" hypothesis but also provide very important observational evidence of the hypothesis (Sohn et al. 2013). The "warm-type precipitation" hypothesis is that heavy precipitation system over the Korean peninsula has lower cloud top height than Oklahoma. Two other previous studies speculated that the warm-type precipitation had deeper liquid cloud layer (called 'feeder zone') and it was developed under moist adiabatically near-neutral condition, based on the TRMM data and weather research and forecast (WRF) model results (Song and Sohn, 2015; Song et al. 2017). We found that the clouds with ML at BSWO was very different from those at SGP when the T_{SFC} is higher than 24 □: lower BLR and higher RD at BSWO than those at SGP. Lower BLR at the BSWO site can be the observational evidence of near-neutral

condition over the Korean peninsula and higher RD can be the evidence of deeper feeder zone.

5. Summary and Conclusions

A QC method for cloud radar data and a melting layer (ML) detection algorithm for cloud radar with linear depolarization ratio (LDR) capability were developed. The QC method was applied to the cloud radar data obtained from the BSWO site and proved to be better than the previously applied method. The ML detection algorithm was found to be universally applicable to the ground-based Ka-band radar data with polarimetric capability. Data collected from the five different sites around the world (SGP, BSWO, ENA, NSA, and OLI) demonstrated that the ML detection method is reliable: the retrieved MLH showed a very good correspondence with the ERA5 zero degree level (ZDL) data for all five sites, showing small negative biases because ice bulb temperature could be lower than 0□. ML detectability was higher for Ka-band radar than for X-band radar (i.e., 8% reduction for X-band), but ML was not detectable with Ka-band radar during heavy precipitation. We expect that the algorithm is highly applicable to other cloud radars which already deployed, such as, dual-frequency dual-polarized Doppler radar (D3R), expanding the knowledge on detailed climatology and physics of ML.

The analyses of long term (about 30 years in total) ML and MLH data for each of the five sites showed contrasting features, revealing some climatological characteristics of clouds and precipitation systems that accompany a melting layer. ML occurrence frequency tended to be high in summer except for a maritime site (ENA), where low stratiform clouds formed frequently in summer, the top of which might be lower than the freezing level. In contrast, at the NSA and OLI sites located in the Arctic region, ML occurred almost exclusively in summer because it was too cold (i.e., subzero temperature at the surface) to have an ML in the other seasons. MLH also varied significantly from site to site but generally was higher during warmer seasons. Based on ML statistics and the newly developed indices, bulk temperature lapse rate (BLR) and relative depth of liquid cloud below MLH (RD), environmental

characteristics at the five sites were investigated. BLR distributed differently for different sites, but showed a general increasing trend with the surface temperature at all sites except ENA that showed an opposing trend, where a unique synoptic pattern in winter generated high BLR in this cold season. SGP and BSWO showed notable differences in BLR characteristics at high temperatures (> 24 □), which were associated with relatively drier but convectively stronger conditions at SGP than at BSWO. This result confirms the "warm-type precipitation" hypothesis suggested by Sohn et al. (2013) with the new observational evidence. Meanwhile, NSA and OLI presented similar statistics due to their proximity. These findings can be used to advance and/or evaluate cumulus parameterization schemes in global climate models (GCMs) (Stephens, 2005; Zhang et al., 2018). Moreover, studies on thermodynamic structures using cloud radars can be broadened and more sophisticated, taking advantage of BLR and RD information, as these indices can represent environmental thermodynamic characteristics of the clouds that have ML. Eventually, further studies can be extended to the assessment of the climatological impact of the clouds with ML.

The primary aim of this study was to characterize the climatology of ML at various locations using cloud radar data, and thus we narrowed our research scope specifically onto the clouds with ML, not onto general convective clouds. On the basis of our aimed scope, we examined detailed statistics of ML occurrences and MLHs, along with ML characteristics at the five sites. Since our approach is different from those of the previous studies on clouds and precipitation in the sense that they mostly focused on precipitating clouds while our study focused on clouds that have ML (e.g., Song et al., 2013; Zhao et al., 2017; Giangrande et al., 2019), there are some gaps between our study and the previous ones. Therefore, it is essential to investigate the characteristics of clouds and precipitation from a comprehensive perspective to fill the gap, and that is the subject of our future study.

Acknowledgments:

This work was funded by the Korea Meteorological Administration Research and

Development Program “Research and Development for KMA weather, climate and Earth system services-Research of Convergence Technology of Forecast and Analysis for Severe Weather” under Grant KMA2018-00121.

Data availability statement:

This study contains modified Copernicus Climate Change Service Information [2020]. Radar data obtained from ARM research facilities (ARMBE datasets) are available through the DOE ARM archive (https://adc.arm.gov/discovery/#/results/primary_meas_type_code::radarreflect/instrument_code::arsclkazr1kollias). The cloud radar data from BSWO used in this study are openly available at Zenodo via https://doi.org/10.5281/zenodo.5153477 (Song, 2021).

Appendix 1. Table of acronyms

Abbreviation	Full name
ARM	Atmspheric Radiation Measurement
ARMBE	ARM best estimation
ARSCL	Active remote sensing of clouds
BLR	Bulk temperature lapse rate
BSWO	Boseong standard weather observatory
CAPE	Convective available potential energy
CFAD	Contoured frequency by altitude diagram
D3R	Dual-frequency dual-polarized Doppler radar
DOE	Department of Energy
EASM	East Asian summer monsoon
ENA	Eastern north Atlantic
ENSO	El Niño southern oscillation
ERA5	ECMWF reanalysis 5
GCM	Global climate model
GPM	Global precipitation measurement
HD(CP)^2	High definition clouds and precipitation for advancing climate precipitation
IQR	Interquartile range
JOYCE	Jülich observatory for cloud evolution
KAZR	Ka-band ARM zenith pointing cloud radar
KMA	Korea meteorological administration
LACROS	Leipzig aerosol and cloud remote observations system
LCL	Lifting condensation level
LDR	Linear depolarization ratio
ML	Melting layer
MLH	Melting layer top height
MMCR	Millimeter wave cloud radar
NIMS	National institute of meteorological sciences
NSA	North slope of Alaska
OLI	Oliktok point
PPI	Plan position indicator
QC	Quality control
R^2	Coefficient of determination
RD	Relative depth of liquid cloud below ML
RH	Relative humidity
RHI	Range height indicator
ρ_{HV}	Copolar correlation coefficient
RMSE	Root mean square error
RSE	Residual standard error
SGP	Southern great plains
T_{SFC}	Surface air temperature
$T_{D,SFC}$	Dewpoint temperature
TRMM	Tropical rain measurement mission
TWP	Tropical western Pacific
V	Vertical velocity
VAP	Value added products
WRF	Weather research and forecast
Z	Radar reflectivity
Z_{DR}	Differential reflectivity
ZDL	Zero degree level

References

Baedi, R., Boers, R., & Russchenberg, H. (2002). Detection of boundary layer water clouds by spaceborne cloud radar. *Journal of Atmospheric and Oceanic Technology*, *19*(12), 1915–1927. https://doi.org/10.1175/1520-0426(2002)019<1915:DOBLWC>2.0.CO;2

Boodoo, S., Hudak, D., Donaldson, N., & Leduc, M. (2010). Application of dual-polarization radar melting-layer detection algorithm. *Journal of Applied Meteorology and Climatology*, *49*(8), 1779–1793. https://doi.org/10.1175/2010JAMC2421.1

Bühl, J., Seifert, P., Wandinger, U., Baars, H., Kanitz, T., Schmidt, J., et al. (2013). LACROS: the Leipzig Aerosol and Cloud Remote Observations System. *Remote Sensing of Clouds and the Atmosphere XVIII; and Optics in Atmospheric Propagation and Adaptive Systems XVI*, *8890*(October 2013), 889002. https://doi.org/10.1117/12.2030911

Carlin, J. T., & Ryzhkov, A. V. (2019). Estimation of melting-layer cooling rate from dual-polarization radar: Spectral bin model simulations. Journal of Applied Meteorology and Climatology, 58(7), 1485-1508.

Cha, J. W., Chang, K. H., Yum, S. S., & Choi, Y. J. (2009). Comparison of the bright band characteristics measured by Micro Rain Radar (MRR) at a mountain and a coastal site in South Korea. *Advances in Atmospheric Sciences*, *26*(2), 211–221. https://doi.org/10.1007/s00376-009-0211-0

Chen, X., & Xie, S. (1994). *ARM: ARMBE: Atmospheric measurements*. Oak Ridge National Lab.(ORNL), Oak Ridge, TN (United States). Atmospheric Radiation Measurement (ARM) Archive. https://doi.org/10.5439/1095313

Clothiaux, E. E., Moran, K. P., Martner, B. E., Ackerman, T. P., Mace, G. G., Uttal, T., et al. (1999). The Atmospheric Radiation Measurement Program cloud radars: Operational modes. *Journal of Atmospheric and Oceanic Technology*, *16*(7), 819–827. https://doi.org/10.1175/1520-0426(1999)016<0819:TARMPC>2.0.CO;2

Clothiaux, E. E., Miller, M. A., Perez, R. C., Turner, D. D., Moran, K. P., Martner, B. E., ... & Ermold, B. (2001). The ARM millimeter wave cloud radars (MMCRs) and the active remote sensing of clouds (ARSCL) value added product (VAP). *Pacific Northwest Natl. Lab.*

Dias Neto, J., Kneifel, S., Ori, D., Trömel, S., Handwerker, J., Bohn, B., ... & Simmer, C. (2019). The TRIple-frequency and Polarimetric radar Experiment for improving process observations of winter precipitation. *Earth System Science Data*, 11(2), 845-863.

Dong, X., Xi, B., Kennedy, A., Minnis, P., & Wood, R. (2014). A 19-month record of marine aerosol-cloud-radiation properties derived from DOE ARM mobile facility deployment at the Azores. Part I: Cloud fraction and single-layered MBL cloud properties. *Journal of Climate*, *27*(10), 3665–3682. https://doi.org/10.1175/JCLI-D-13-00553.1

Fabry, F., & Zawadzki, I. (1995). Long-term radar observations of the melting layer of precipitation and their interpretation. *Journal of Atmospheric Sciences*, *52*(7), 838-851.

Frisch, A. S., Fairall, C. W., & Snider, J. B. (1995). Measurement of Stratus Cloud and Drizzle Parameters in ASTEX with a K α -Band Doppler Radar and a Microwave Radiometer. *Journal of the Atmospheric Sciences*. *52*(16), 2788–2799. https://doi.org/10.1175/1520-0469(1995)052<2788:moscad>2.0.co;2

Gao, J., Tang, G., & Hong, Y. (2017). Similarities and improvements of GPM dual-frequency precipitation radar (DPR) upon TRMM precipitation radar (PR) in global precipitation rate estimation, type classification and vertical profiling. *Remote Sensing*, *9*(11), 1–26. https://doi.org/10.3390/rs9111142

Giangrande, S. E., Krause, J. M., & Ryzhkov, A. V. (2008). Automatic designation of the melting layer with a polarimetric prototype of the WSR-88D radar. *Journal of Applied Meteorology and Climatology*, *47*(5), 1354–1364. https://doi.org/10.1175/2007JAMC1634.1

Giangrande, S. E., Wang, D., Bartholomew, M. J., Jensen, M. P., Mechem, D. B., Hardin, J. C., & Wood, R. (2019). Midlatitude Oceanic Cloud and Precipitation Properties as Sampled by the ARM Eastern North Atlantic Observatory. *Journal of Geophysical Research Atmospheres, 124*(8), 4741–4760. https://doi.org/10.1029/2018JD029667

Gunn, R., & Kinzer, G. D. (1949). the Terminal Velocity of Fall for Water Droplets in Stagnant Air. *Journal of Meteorology*. https://doi.org/10.1175/1520-0469(1949)006<0243:ttvoff>2.0.co;2

Heymsfield, A. J., Bansemer, A., Theis, A., & Schmitt, C. (2021). Survival of Snow in the Melting Layer: Relative Humidity Influence, *Journal of the Atmospheric Sciences,* doi.org/10.1175/JAS-D-20-0353.1 (published online).

Hogan, R. J., & O'Connor, E. J. (2004). Facilitating cloud radar and lidar algorithms: the Cloudnet Instrument Synergy/Target Categorization product. *Cloudnet documentation, 14.*

Ikeda, K., Brandes, E. A., & Rasmussen, R. M. (2005). NOTES AND CORRESPONDENCE: Polarimetric Radar Observation of Multiple Freezing Levels, *Journal of the Atmospheric Sciences, 62*(10), 3624-3636.

Jensen, M. (2012). *ARM KAZR-ARSCL Value Added Product*. Oak Ridge National Lab.(ORNL), Oak Ridge, TN (United States). Atmospheric Radiation Measurement (ARM) Archive. https://doi.org/10.5439/1052058

Khain, A., Rosenfeld, D., & Pokrovsky, A. (2005). Aerosol impact on the dynamics and microphysics of deep convective clouds. *Quarterly Journal of the Royal Meteorological Society*, *131*(611), 2639–2663. https://doi.org/10.1256/qj.04.62

Kim, H. W., & Lee, D. K. (2006). An observational study of mesoscale convective systems with heavy rainfall over the Korean Peninsula. *Weather and Forecasting*, *21*(2), 125–148. https://doi.org/10.1175/WAF912.1

Kodama, Y. M., Katsumata, M., Mori, S., Satoh, S., Hirose, Y., & Ueda, H. (2009). Climatology of warm rain and associated latent heating derived from TRMM PR observations. *Journal of Climate*, *22*(18), 4908–4929. https://doi.org/10.1175/2009JCLI2575.1

Kollias, P., & Albrecht, B. (2000). The turbulence structure in a continental stratocumulus cloud from millimeter-wavelength radar observations. *Journal of the Atmospheric Sciences*, *57*(15), 2417–2434. https://doi.org/10.1175/1520-0469(2000)057<2417:TTSIAC>2.0.CO;2

Kollias, P., Albrecht, B. A., Lhermitte, R., & Savtchenko, A. (2001). Radar observations of updrafts, downdrafts, and turbulence in fair-weather cumuli. *Journal of the Atmospheric Sciences*, *58*(13), 1750–1766. https://doi.org/10.1175/1520-0469(2001)058<1750:ROOUDA>2.0.CO;2

Kollias, P., Albrecht, B. A., & Marks, F. (2002). Why mie? Accurate observations of vertical air velocities and raindrops using a cloud radar. *Bulletin of the American Meteorological Society*, *83*(10), 1471-1483+1438. https://doi.org/10.1175/BAMS-83-10-1471

Kollias, P., & Albrecht, B. (2005). Why the melting layer radar reflectivity is not bright at 94 GHz. *Geophysical research letters*, *32*(24).

Kollias, P., Clothiaux, E. E., Miller, M. A., Luke, E. P., Johnson, K. L., Moran, K. P., et al. (2007). The atmospheric radiation measurement program cloud profiling radars: Second-generation sampling strategies, processing, and cloud data products. *Journal of Atmospheric and Oceanic Technology*, *24*(7), 1199–1214. https://doi.org/10.1175/JTECH2033.1

Lau, K. M., Yang, G. J., & Shen, S. H. (1988). Seasonal and intraseasonal climatology of summer monsoon rainfall over East Asia. *Monthly Weather Review*. https://doi.org/10.1175/1520-0493(1988)116<0018:SAICOS>2.0.CO;2

Le, M., & Chandrasekar, V. (2012). Precipitation type classification method for dual-frequency precipitation radar (DPR) onboard the GPM. *IEEE transactions on geoscience and remote sensing*, *51*(3), 1784-1790.

Li, H., & Moisseev, D. (2020). Two layers of melting ice particles within a single radar bright band: Interpretation and implications. *Geophysical Research Letters*, 47(13), e2020GL087499.

Liu, Y., Geerts, B., Miller, M., Daum, P., & McGraw, R. (2008). Threshold radar reflectivity for drizzling clouds. *Geophysical Research Letters*, *35*(3), 1–5. https://doi.org/10.1029/2007GL031201

Löhnert, U., Schween, J. H., Acquistapace, C., Ebell, K., Maahn, M., Barrera-Verdejo, M., et al. (2015). JOYCE: Jülich Observatory for Cloud Evolution. *Bulletin of the American Meteorological Society*, *96*(7), 1157–1174. https://doi.org/10.1175/BAMS-D-14-00105.1

Luke, E. P., & Kollias, P. (2013). Separating cloud and drizzle radar moments during precipitation onset using doppler spectra. *Journal of Atmospheric and Oceanic Technology*, *30*(8), 1656–1671. https://doi.org/10.1175/JTECH-D-11-00195.1

Mace, G. G., & Sassen, K. (2000). A constrained algorithm for retrieval of stratocumulus cloud properties using solar radiation, microwave radiometer, and millimeter cloud radar data. Journal of Geophysical Research: Atmospheres, 105(D23), 29099-29108.

Mather, J. H., & Voyles, J. W. (2013). The arm climate research facility: A review of structure and capabilities. *Bulletin of the American Meteorological Society*, *94*(3), 377–392. https://doi.org/10.1175/BAMS-D-11-00218.1

Matrosov, S. Y. (2005). Attenuation-based estimates of rainfall rates aloft with vertically pointing Ka-band radars. *Journal of Atmospheric and Oceanic Technology*, *22*(1), 43–54. https://doi.org/10.1175/JTECH-1677.1

Matrosov, S. Y. (2008). Assessment of radar signal attenuation caused by the melting hydrometeor layer. *IEEE Transactions on Geoscience and Remote Sensing*, *46*(4), 1039–1047. https://doi.org/10.1109/TGRS.2008.915757

Matrosov, S. Y., Cifelli, R., White, A., & Coleman, T. (2017). Snow-Level Estimates Using Operational Polarimetric Weather Radar Measurements, *Journal of Hydrometeorology*, *18*(4), 1009-1019.

Miller, M. A., Nitschke, K., Ackerman, T. P., Ferrell, W. R., Hickmon, N., & Ivey, M. (2016). The ARM Mobile Facilities. *Meteorological Monographs*, *57*, 9.1-9.15. https://doi.org/10.1175/amsmonographs-d-15-0051.1

Oh, S. B., Kim, Y. H., Kim, K. H., Cho, C. H., & Lim, E. (2016). Verification and correction of cloud base and top height retrievals from Ka-band cloud radar in Boseong, Korea. *Advances in Atmospheric Sciences*, *33*(1), 73–84. https://doi.org/10.1007/s00376-015-5058-y

Oh, S. B., Lee, Y. H., Jeong, J. H., Kim, Y. H., & Joo, S. (2018). Estimation of the liquid water content and Z–LWC relationship using Ka-band cloud radar and a microwave radiometer. *Meteorological Applications*, *25*(3), 423–434. https://doi.org/10.1002/met.1710

Oh, S. B., Kollias, P., Lee, J. S., Lee, S. W., Lee, Y. H., & Jeong, J. H. (2019). Rain-rate estimation algorithm using signal attenuation of Ka-band cloud radar. *Meteorological Applications*, (August 2019), 1–13. https://doi.org/10.1002/met.1825

Romps, D. M. (2017). Exact expression for the lifting condensation level. *Journal of the Atmospheric Sciences*, *74*(12), 3891-3900.

Sassen, K., Matrosov, S., & Campbell, J. (2007). CloudSat spaceborne 94 GHz radar bright bands in the melting layer: An attenuation- driven upside- down lidar analog. Geophysical research letters, 34(16).

Sato, K., & Okamoto, H. (2006). Characterization of Ze and LDR of nonspherical and inhomogeneous ice particles for 95-GHz cloud radar: Its implication to microphysical retrievals. *Journal of Geophysical Research Atmospheres*, *111*(22), 1–15. https://doi.org/10.1029/2005JD006959

Sauvageot, H., & Omar, J. (1987). Radar Reflectivity of Cumulus Clouds. *Journal of Atmospheric and Oceanic Technology*. https://doi.org/10.1175/1520-0426(1987)004<0264:rrocc>2.0.co;2

Shin, D. B., North, G. R., & Bowman, K. P. (2000). A summary of reflectivity profiles from the first year of TRMM radar data. *Journal of Climate*, *13*(23), 4072–4086. https://doi.org/10.1175/1520-0442(2000)013<4072:ASORPF>2.0.CO;2

Shin, C. S., & Lee, T. Y. (2005). Development mechanisms for the heavy rainfalls of 6-7 August 2002 over the middle of the Korean Peninsula. *Journal of the Meteorological Society of Japan*, *83*(5), 683–709. https://doi.org/10.2151/jmsj.83.683

Shupe, M. D. (2007). A ground- based multisensor cloud phase classifier. Geophysical Research Letters, 34(22).

Shupe, M. D., Walden, V. P., Eloranta, E., Uttal, T., Campbell, J. R., Starkweather, S. M., & Shiobara, M. (2011). Clouds at Arctic atmospheric observatories. Part I: Occurrence and macrophysical properties. *Journal of Applied Meteorology and Climatology*, 50(3), 626–644. https://doi.org/10.1175/2010JAMC2467.1

Sohn, B. J., Ryu, G. H., Song, H. J., & Ou, M. L. (2013). Characteristic features of warm-type rain producing heavy rainfall over the Korean peninsula inferred from TRMM measurements. *Monthly Weather Review*, *141*(11), 3873–3888. https://doi.org/10.1175/MWR-D-13-00075.1

Sokol, Z., Minářová, J., & Novák, P. (2018). Classification of hydrometeors using measurements of the ka-band cloud radar installed at the Milešovka Mountain (Central Europe). *Remote Sensing*, *10*(11). https://doi.org/10.3390/rs10111674

Song, H. J., & Sohn, B. J. (2015). Two heavy rainfall types over the Korean Peninsula in the humid East Asian summer environment: A satellite observation study. *Monthly Weather Review*, *143*(1), 363–382. https://doi.org/10.1175/MWR-D-14-00184.1

Song, H. J., Sohn, B. J., Hong, S. Y., & Hashino, T. (2017). Idealized numerical experiments on the microphysical evolution of warm-type heavy rainfall. *Journal of Geophysical Research Atmospheres*, *122*(3), 1685–1699. https://doi.org/10.1002/2016JD025637

Stephens, G. L. (2005). Cloud feedbacks in the climate system: A critical review. *Journal of Climate*, *18*(2), 237–273. https://doi.org/10.1175/JCLI-3243.1

Wang, B., & Lin, H. (2002). Rainy season of the Asian-Pacific summer monsoon. *Journal of Climate*, *15*(4), 386–398. https://doi.org/10.1175/1520-0442(2002)015<0386:RSOTAP>2.0.CO;2

Widener, K., Bharadwaj, N., & Johnson, K. (2012). *Ka-Band ARM Zenith Radar (KAZR) Instrument Handbook*. United States. https://doi.org/10.2172/1035855

Wolfensberger, D., Scipion, D., & Berne, A. (2016). Detection and characterization of the melting layer based on polarimetric radar scans. *Quarterly Journal of the Royal Meteorological Society*, *142*, 108-124.

Wood, C. R., O'Connor, E. J., Hurley, R. A., Reynolds, D. R., & Illingworth, A. J. (2009). Cloud-radar observations of insects in the UK convective boundary layer. Meteorological Applications: A journal of forecasting, practical applications, training techniques and modelling, 16(4), 491-500.

Wood, R., Wyant, M., Bretherton, C. S., Rémillard, J., Kollias, P., Fletcher, J., et al. (2015). Clouds, aerosols, and precipitation in the marine boundary layer: An arm mobile facility deployment. *Bulletin of the American Meteorological Society*, *96*(3), 419–439. https://doi.org/10.1175/BAMS-D-13-00180.1

Yihui, D., & Chan, J. C. L. (2005). The East Asian summer monsoon: An overview. *Meteorology and Atmospheric Physics*, *89*(1–4), 117–142. https://doi.org/10.1007/s00703-005-0125-z

Zhang, Y. Y., Xie, S., Klein, S. A., MaRchand, R. R., KolliaS, P., Clothiaux, E. E., et al. (2018). The ARM cloud radar simulator for global climate models bridging field data and climate models. *Bulletin of the American Meteorological Society, 99*(1), 21–26. https://doi.org/10.1175/BAMS-D-16-0258.1

Zhao, W., Marchand, R., & Fu, Q. (2017). The diurnal cycle of clouds and precipitation at the ARM SGP site: Cloud radar observations and simulations from the multiscale modeling framework. *Journal of Geophysical Research Atmospheres*, *122*(14), 7519–7536. https://doi.org/10.1002/2016JD026353

Table 1. Criteria used for the QC method based on the physical limits of the hydrometeor particles.

Criterion	Variable	Lower threshold	Upper threshold
Low cloud (< 3 km)	Z	-	-25 dBZ
	V	-1 m s^{-1}	1 m s^{-1}
	LDR	-	-15dB
Liquid cloud	Z	-	0 dBZ
	V	-5 m s^{-1}	5 m s^{-1}
	LDR	-	-15 dB
Ice cloud	Z	0 dBZ	-
	V	-10 m s^{-1}	5 m s^{-1}
	LDR	-	-5 dB
Light precipitation (<3 km)	Z	-15 dBZ	0 dBZ
	V	-5 m s^{-1}	5 m s^{-1}
	LDR	-	-15 dB
Heavy precipitation (<3 km)	Z	0	-
	V	-10 m s^{-1}	5 m s^{-1}
	LDR	-	-5 dB

Table 2. Total and ML observed time in hours.

Site	Total hours	ML observed hours
SGP	51309	1427
BSWO	6246	696
ENA	29795	485
NSA	55433	1680
OLI	18127	617

Table 3. Slopes, intercepts, R^2s, and RSEs of the regression lines presented in Figs. 11 - 14.

	T_{SFC} vs BLR (Fig. 11)				RH vs RD (Fig. 12)				T_{SFC} vs RD (Fig. 13)				RD vs BLR (Fig. 14)			
Site	Slope (km^{-1})	Intercept ($\square$ km^{-1})	R^2	RSE ($\square$ km^{-1})	Slope (10^{-3} $\%^{-1}$)	Intercept (10^{-3})	R^2	RSE	Slope (10^{-3} $\square^{-1}$)	Intercept (10^{-3})	R^2	RSE	Slope ($\square$ km^{-1})	Intercept ($\square$ km^{-1})	R^2	RSE ($\square$ km^{-1})
SGP	0.18	1.6	0.91	2.22	9.12	125	0.94	0.14	-0.43	894	0.03	0.04	-3.8	8.1	0.80	1.67
BSW O	0.14	2.1	0.53	1.75	9.61	107	0.94	0.21	9.85	643	0.28	0.14	-3.25	7.6	0.93	2.50
ENA	-0.19	9.6	0.75	2.76	7.79	213	1.00	0.12	14.6	592	0.81	0.05	-7.7	12.7	1.00	2.06
NSA	0.39	0.72	0.98	1.76	10.9	-70	1.00	0.13	-4.41	977	0.53	0.07	-9.6	11.2	1.00	2.35
OLI	0.42	0.58	0.97	2.59	6.29	305	0.93	0.05	-1.39	869	0.07	0.03	-9.0	10.4	0.96	2.43

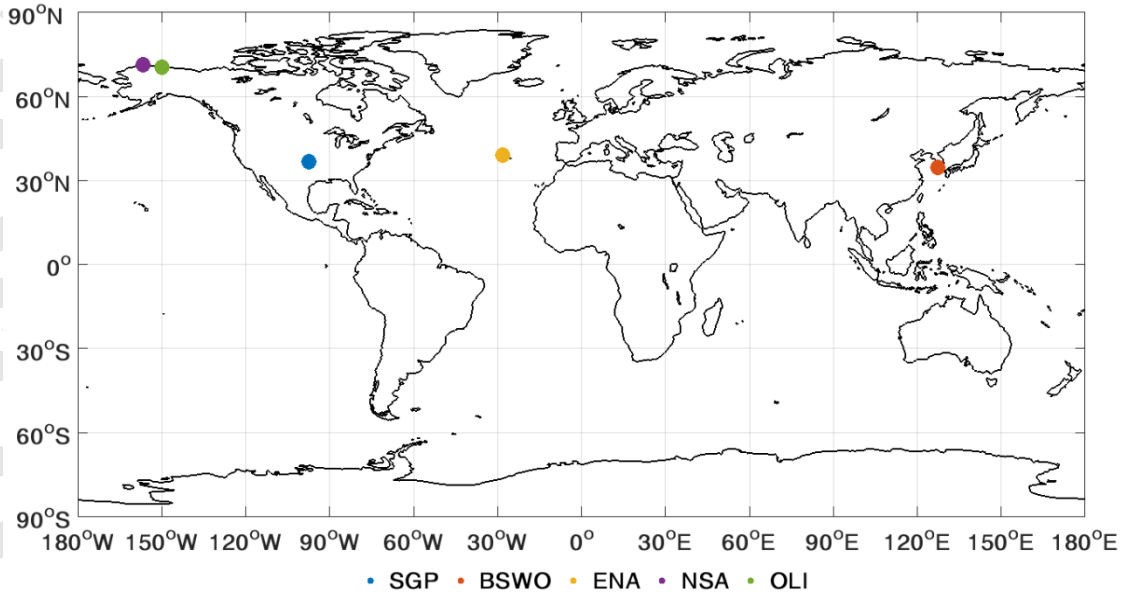

Figure 1. Locations of the cloud radar observation sites examined in this study.

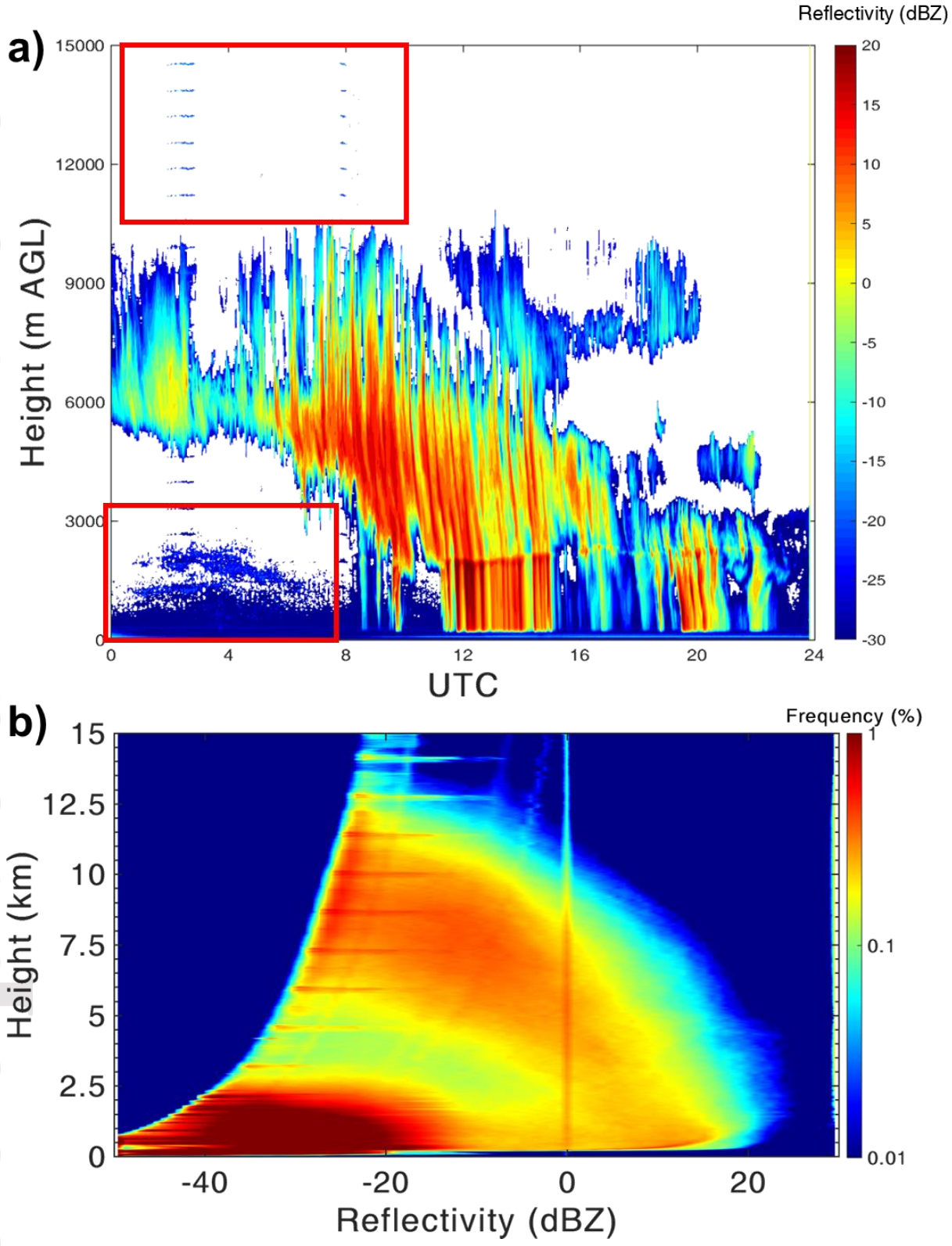

Figure 2. Time series of radar moment data before QC at BSWO on April 12, 2015 (a), and CFAD of all cloud radar data at BSWO used in this study without applying a QC method (b). Red box indicates band-shaped noises and ground clutters.

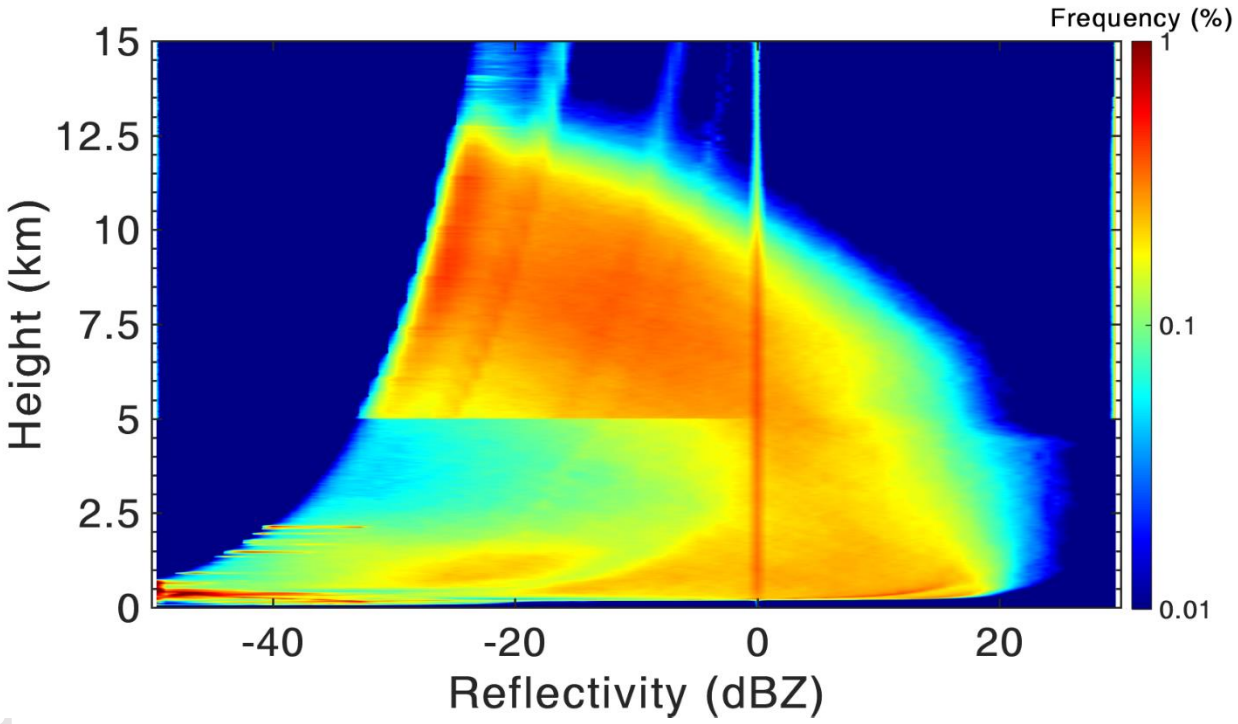

Figure 3. CFAD of BSWO cloud radar data with the application of the QC method introduced by Oh et al. (2018).

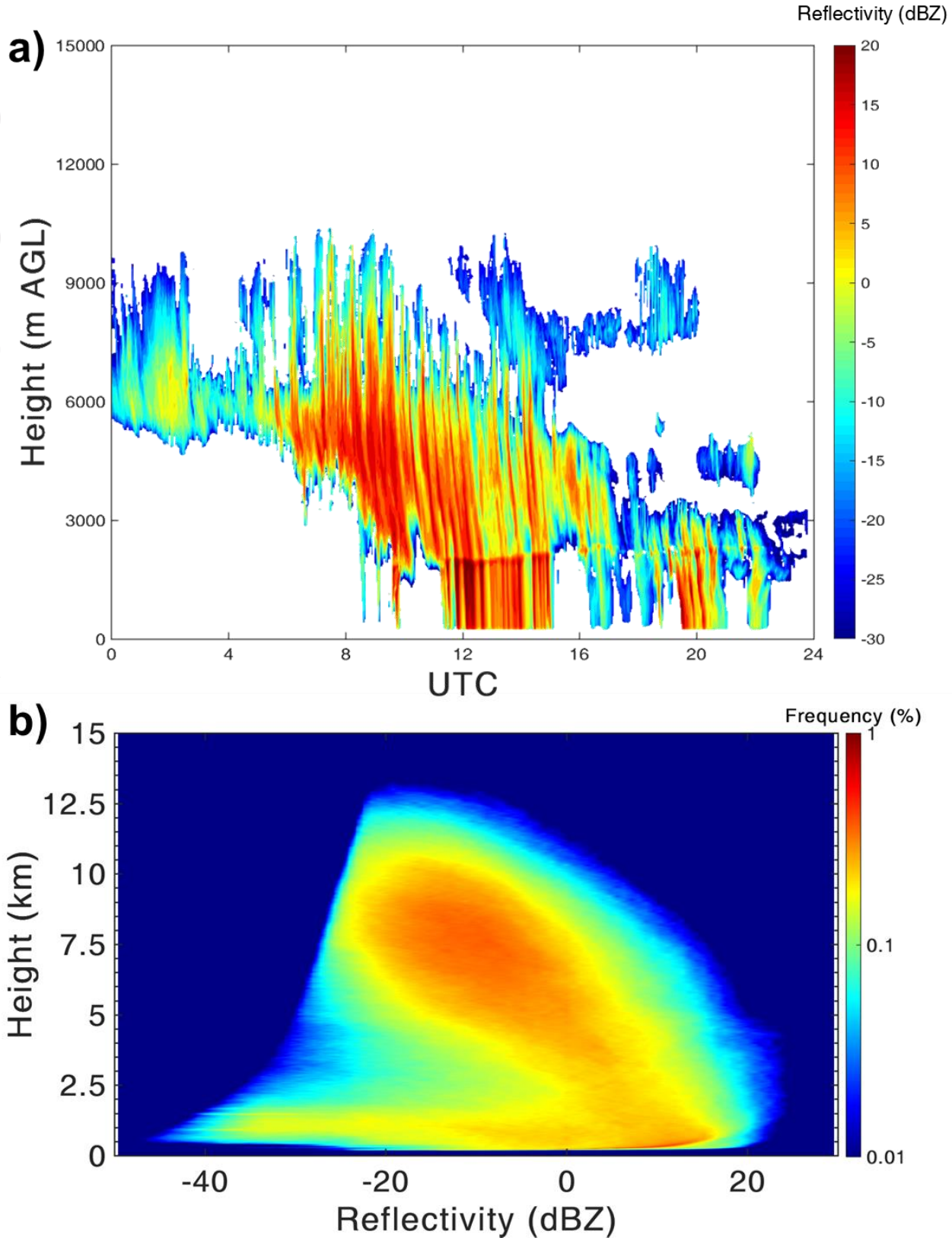

Figure 4. Same as Fig. 2, but after the new QC method was applied.

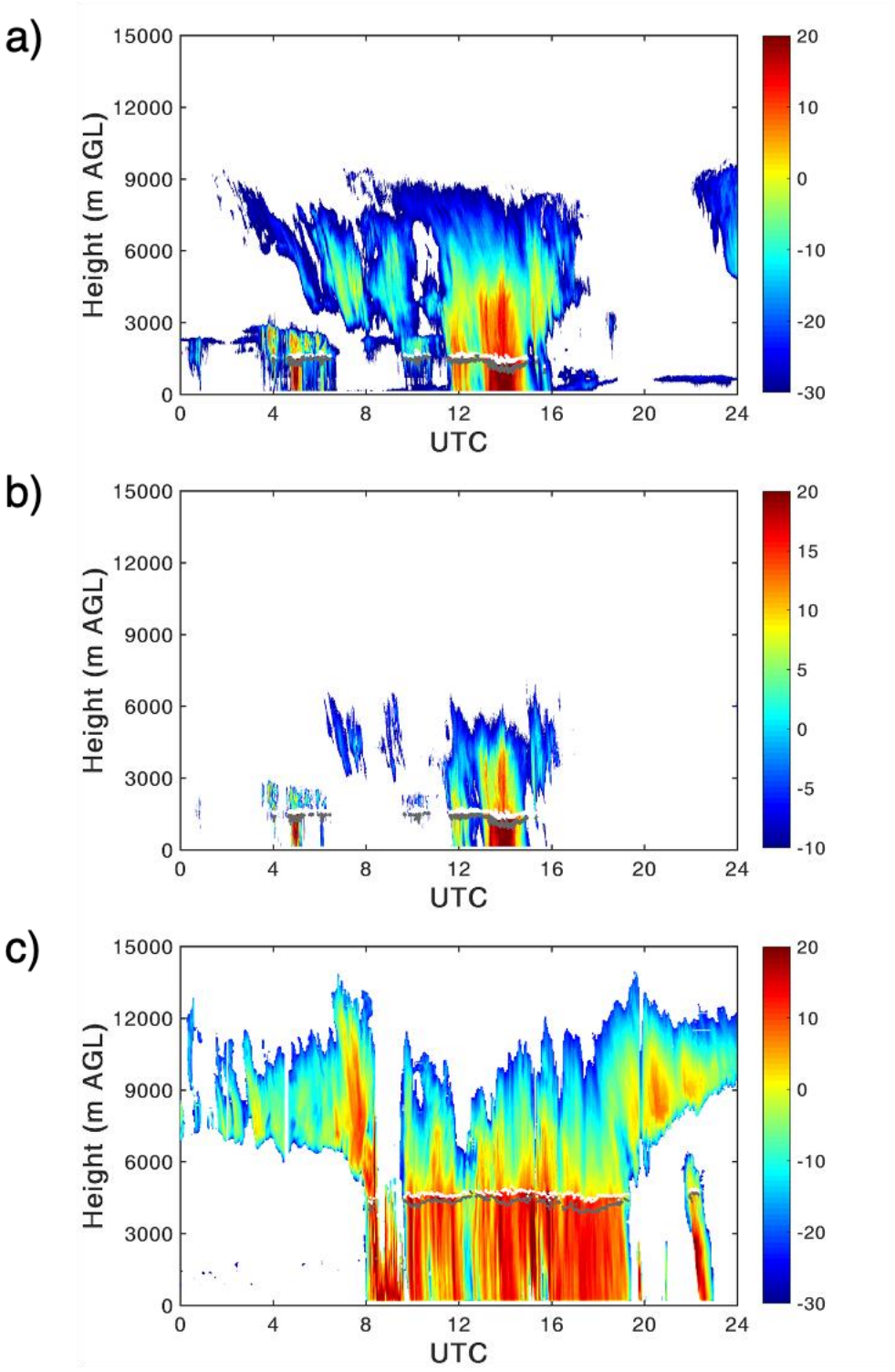

Figure 5. (a) Time series of the cloud radar data at NSA on September 12, 2013. White and grey dots indicate the ML top and bottom, respectively. Shaded color in each figure indicates reflectivity in dBZ. (b) Same as (a) but only for Z > -10 dBZ. (c) same as (a) but for the case at BSWO on July 17, 2017.

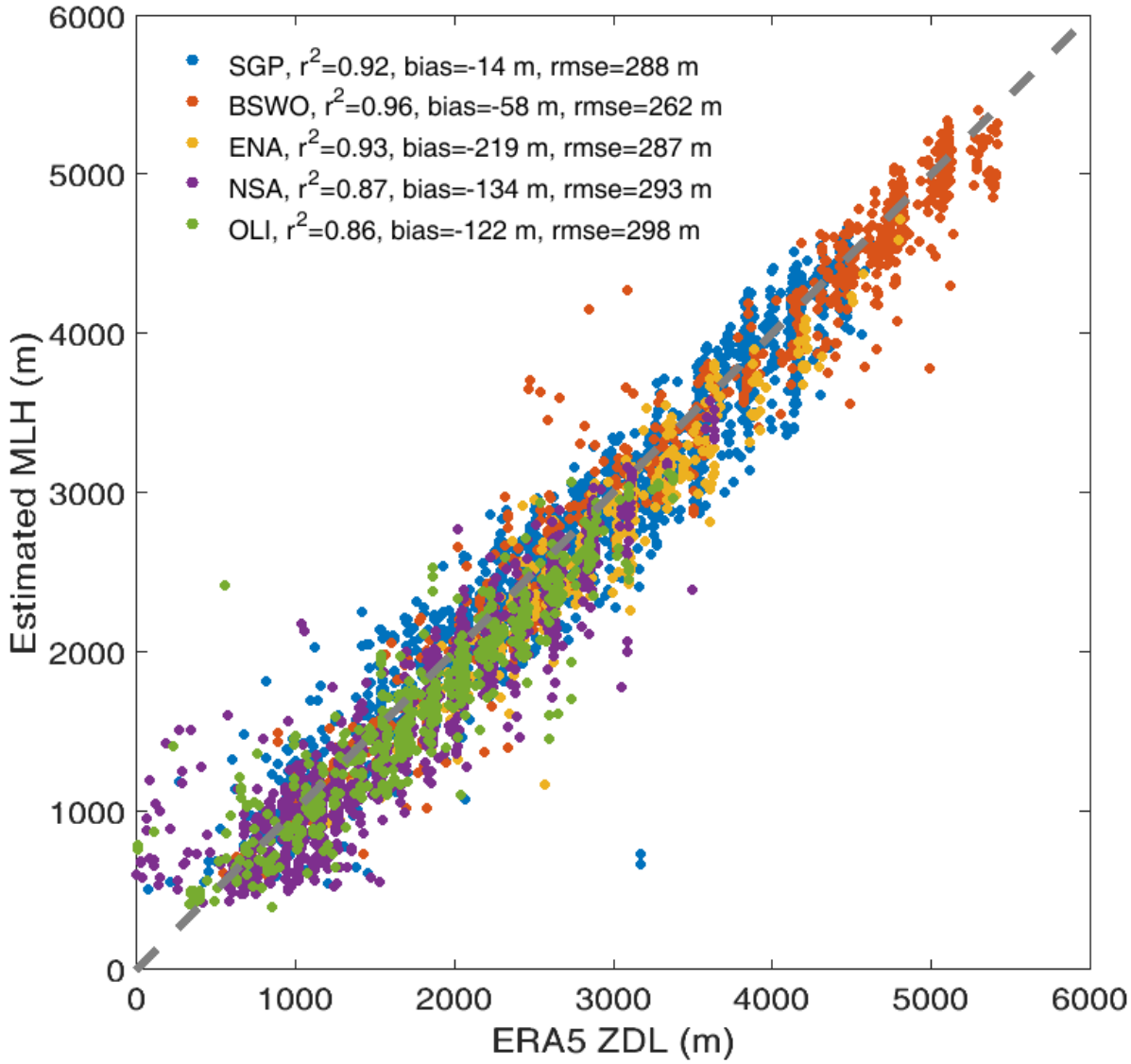

Figure 6. ZDL data of ERA5 versus ML top heights retrieved by the ML detection method developed in this study. Coefficient of determination (r^2), bias and RMSE are presented in the figure.

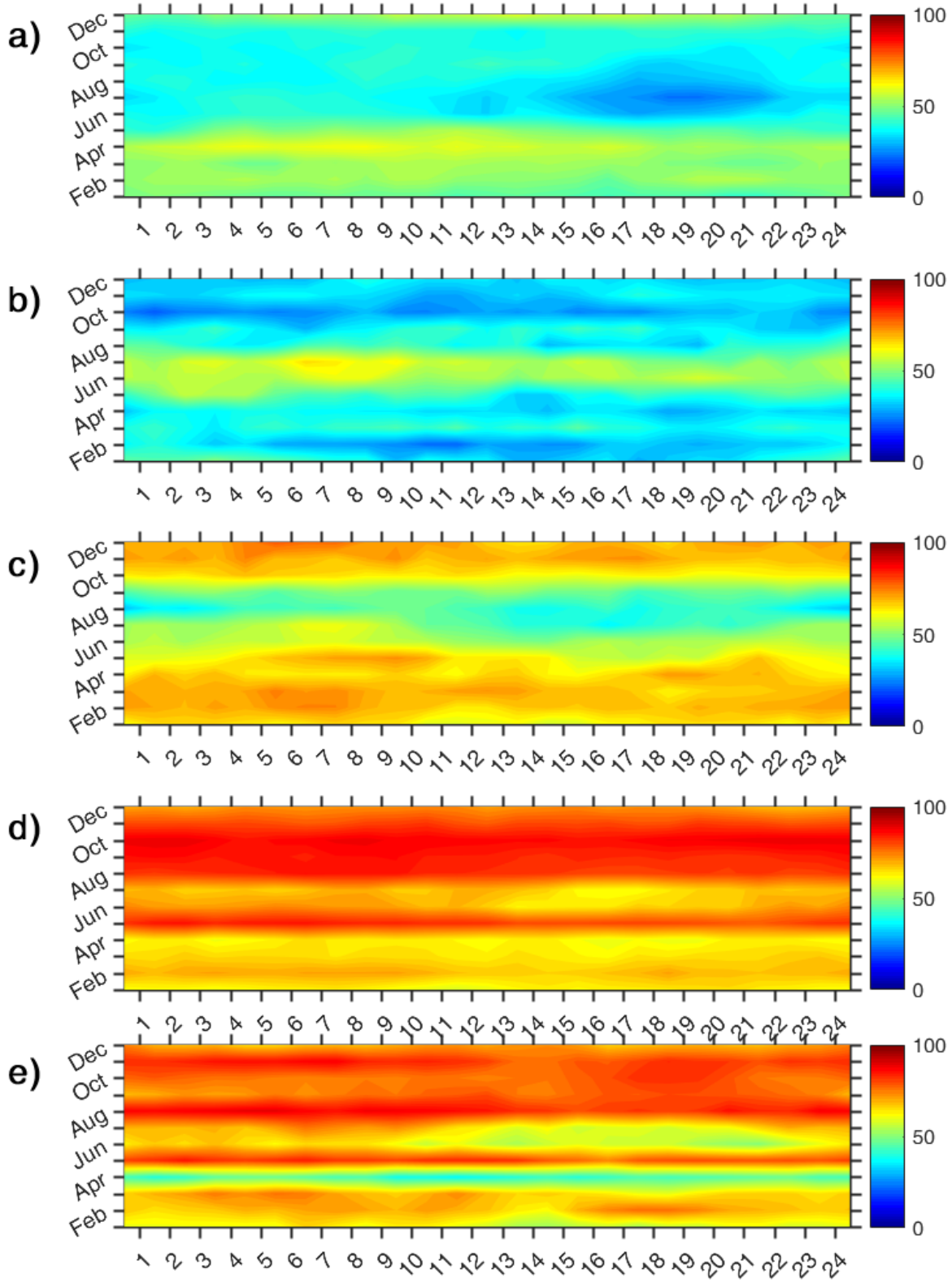

Figure 7. Monthly and hourly occurrence frequencies (%) of clouds at SGP (a), BSWO (b), ENA (c), NSA (d), and OLI (e). The x and y axes indicate Local Standard Time (LST) and month, respectively.

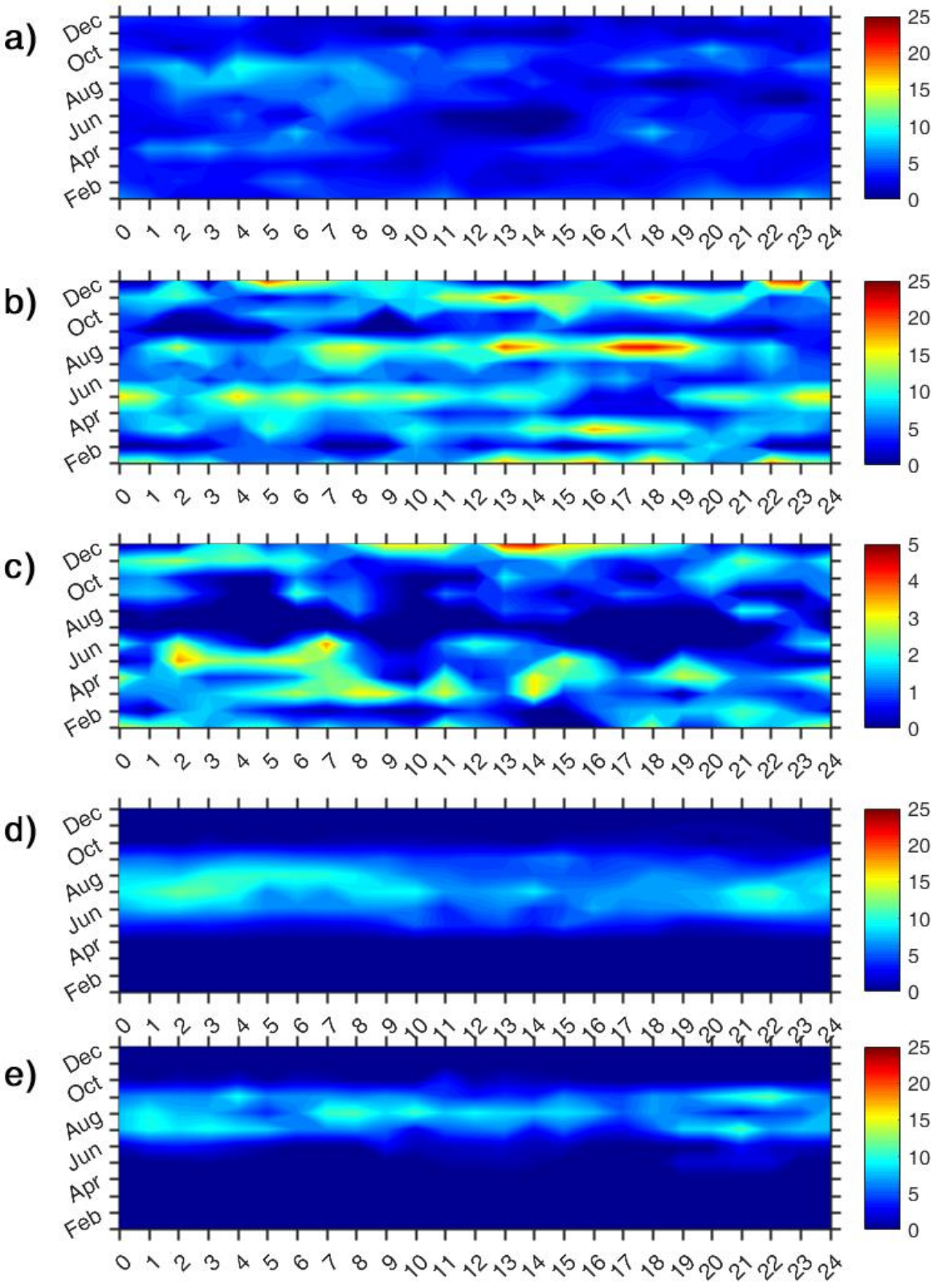

Figure 8. ML occurrence frequency (%) shown as the ratio of the number of ML occurrence to the number of observations that detected clouds.

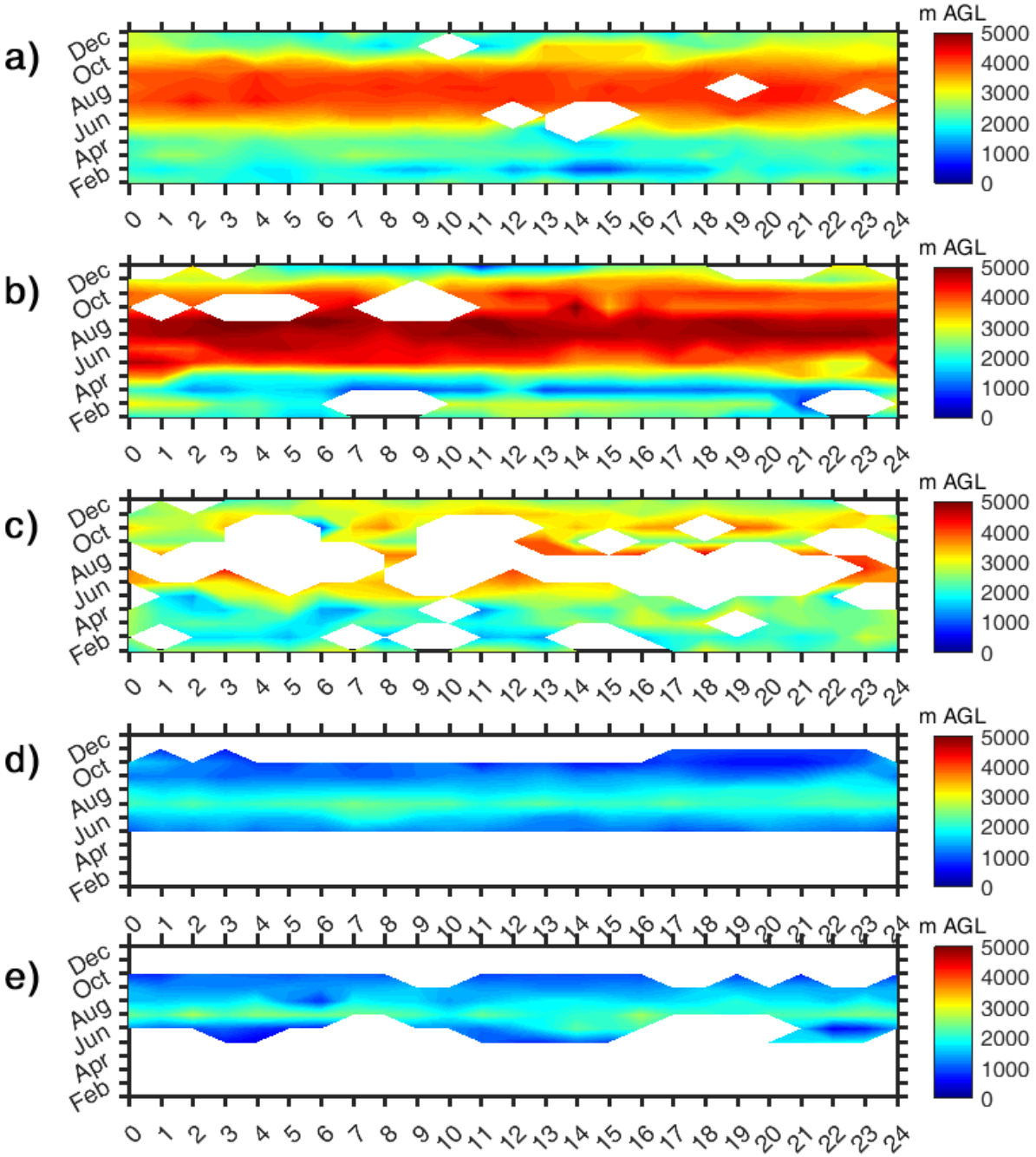

Figure 9. Monthly and hourly averaged MLH at SGP (a), BSWO(b), ENA (c), NSA (d), and OLI (e). The white color areas indicate the time of ML absence.

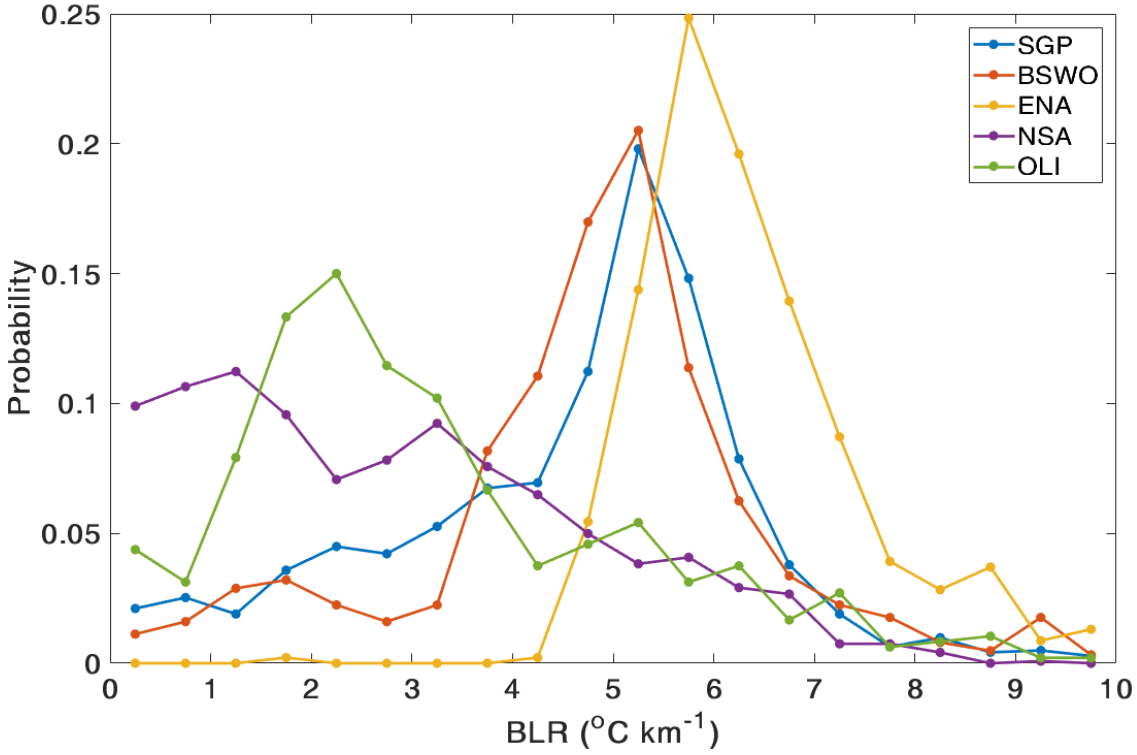

Figure 10. Histogram of BLR at the five sites.

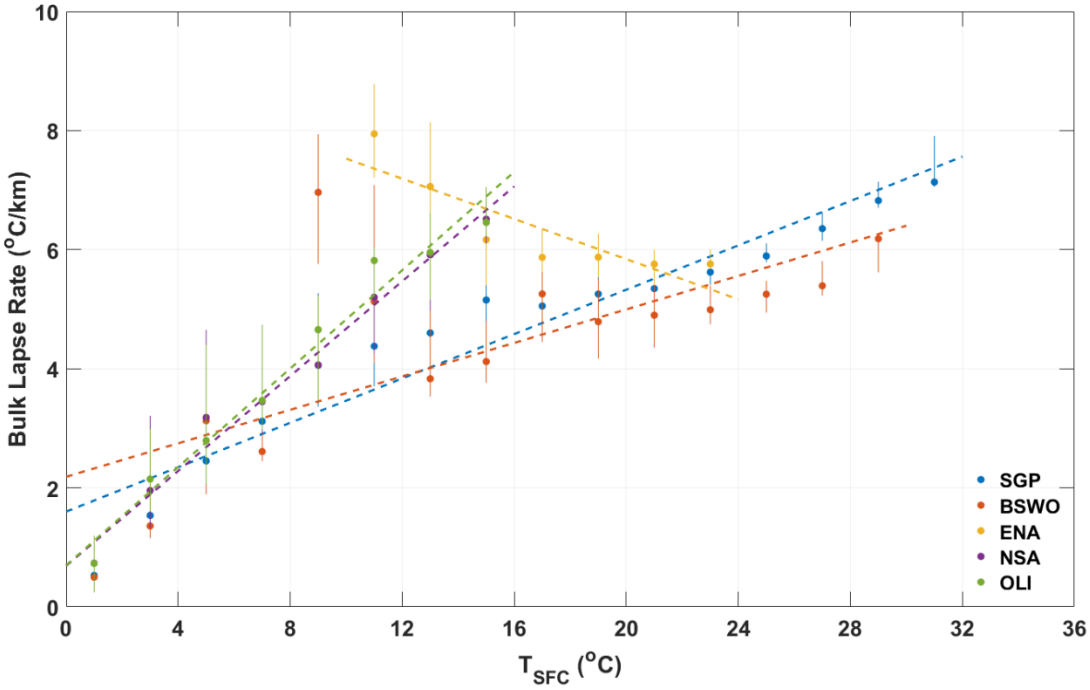

Figure 11. T_{SFC} versus BLR for all sites. Bars and circles indicate IQR, and median respectively. The dashed lines are the regression lines for the median BLR for each T_{SFC} bin (2 □).

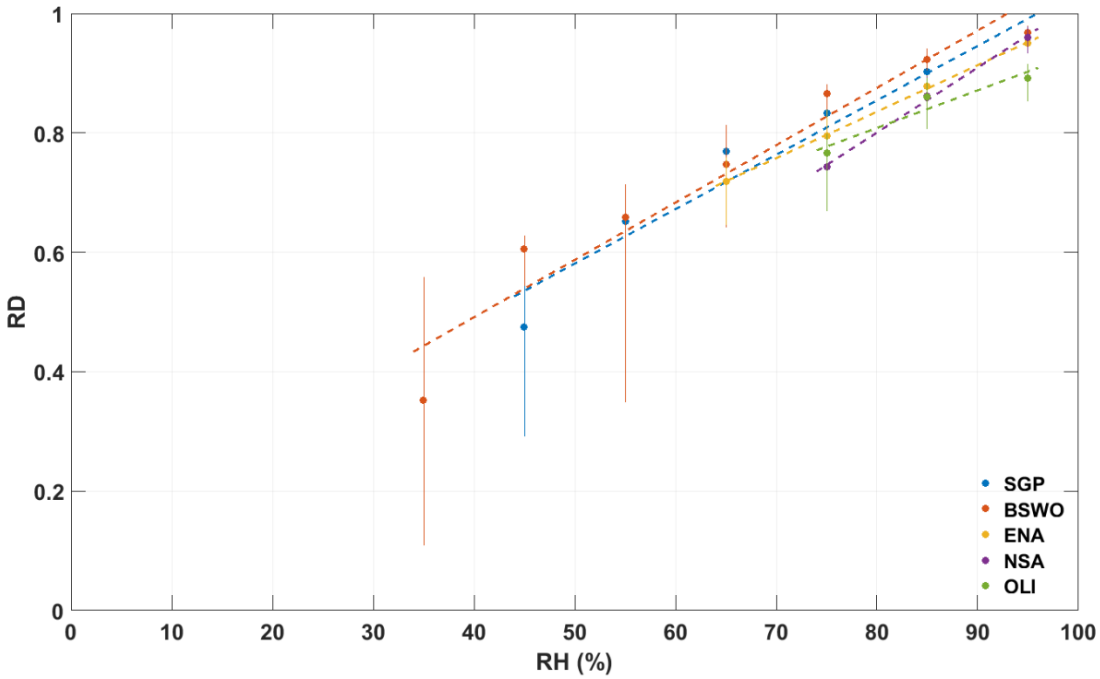

Figure 12. Same as Fig. 11 but for RH versus RD. The dashed lines are the regression lines for the median of RD for each RH bin (10 %).

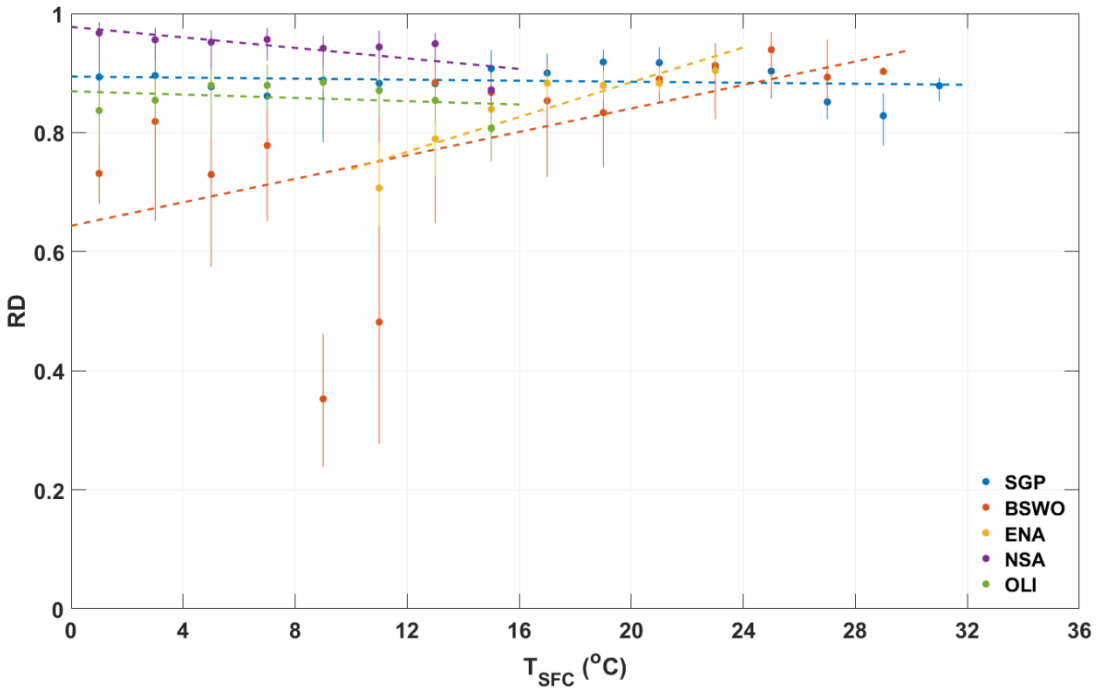

Figure 13. Same as Fig. 11 but for T_{SFC} versus RD. The dashed lines are the regression lines for the median of RD for each T_{SFC} bin (2 □).

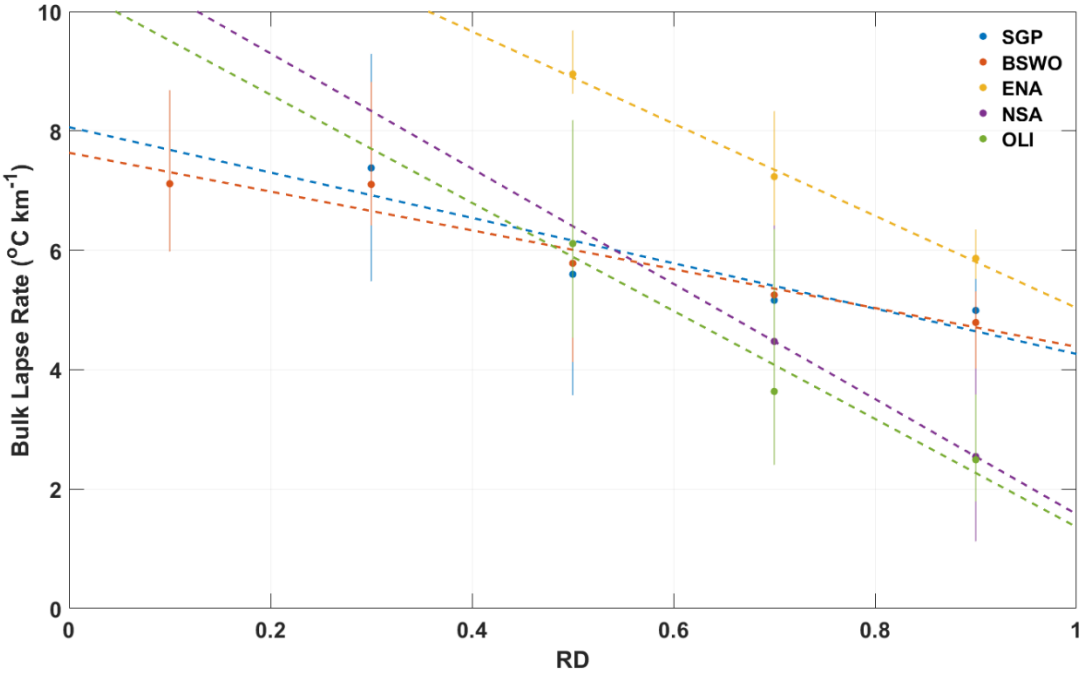

Figure 14. Same as Fig. 11 but for RD versus BLR. The dashed lines are the regression lines for the median of BLR for each RD bin (0.2).